Probabilistic Assessment of the Lifetime of Low-Earth-Orbit Spacecraft: Uncertainty Characterization

Lamberto Dell'Elce,[*] Maarten Arnst,[†] and Gaëtan Kerschen[‡]
University of Liège, 4000 Liège, Belgium

Orbital lifetime estimation is a problem of great timeliness and importance in astrodynamics. In view of the stochastic nature of the thermosphere and of the complexity of drag modeling, any deterministic assessment of orbital lifetime is likely to be bound to failure. This is why the present paper performs uncertainty quantification of satellite orbital lifetime estimation. Specifically, this paper focuses on the probabilistic characterization of the dominant sources of uncertainty inherent to low-altitude satellites. Uncertainties in the initial state of the satellite and in the atmospheric drag force, as well as uncertainties introduced by modeling limitations associated with atmospheric density models, are considered. Mathematical statistics methods, in conjunction with mechanical modeling considerations, are used to infer the probabilistic characterization of these uncertainties from experimental data and atmospheric density models. This characterization step facilitates the application of uncertainty propagation and sensitivity analysis methods, which in turn allows gaining insight into the impact that these uncertainties have on the orbital lifetime. The proposed developments are illustrated using one CubeSat of the QB50 constellation.

Nomenclature

A	=	surface, m^2
A_p	=	geomagnetic activity index, deg
B	=	Boltzmann constant, J/K
C_b	=	ballistic coefficient, m^2/kg
C_d	=	drag coefficient
c_N	=	cumulative distribution function of a standard normal random variable
d	=	number of parameters of a generic probability density function
e	=	orbital eccentricity
$\mathcal{F}$	=	cumulative distribution function of a random variable
$F_{10.7}$	=	daily solar radio flux, sfu
$\bar{F}_{10.7}$	=	81-day averaged solar radio flux, sfu
$\boldsymbol{f}$	=	force per mass unit, N/kg
$\boldsymbol{g}, \boldsymbol{z}$	=	generic vectorial functions
h	=	spacecraft altitude from the equatorial radius, m
I	=	support of a random variable
i	=	orbital inclination, deg
L	=	likelihood function
m	=	mass of the spacecraft, kg
m_j	=	molecular mass of the gas species j, g/mol
n	=	number of samples
n_j	=	number density of the gas species j, m^{-3}
p	=	probability density function of a random variable
$\boldsymbol{p}$	=	vector of parameters
p_N	=	standard normal distribution
$\boldsymbol{q}$	=	quaternion defining the attitude of the spacecraft
$\boldsymbol{r}$	=	position in the Earth centered inertial frame, m
R	=	universal gas constant, J/molK
s	=	entropy of a random variable
T	=	local atmospheric temperature, K
T_w	=	wall temperature, K
t	=	time, s
U	=	uniform random variable defined on [0,1]
$\boldsymbol{v}$	=	velocity in the Earth centered inertial frame, m/s
v_{ej}	=	norm of the ejection velocity, m/s
v_{inc}	=	incident velocity, m/s
$v_{mp,j}$	=	most probable thermal velocity of the gas species j, m/s
v_{re}	=	reemitted velocity, m/s
v_{TAS}	=	true airspeed of spacecraft, m/s
W	=	bulk velocity to most probable thermal velocity ratio
x	=	generic deterministic variable
X	=	generic random variable
Z, Ψ	=	standard Gaussian random variable
α	=	energy accommodation coefficient
β	=	bias error of a numerical model
δ	=	angle of attack, deg
ϵ	=	roll angle, deg
η	=	model error of a numerical model (stochastic variable)
Θ	=	spherical angle (azimuth) of the ejection velocity, deg
μ	=	mean value of a random variable
ν	=	Earth gravitational constant, m^{3}s^{-2}
ρ	=	atmospheric density, kg/m^3
σ	=	standard deviation of a random variable
φ	=	linear shape function
ψ_k	=	angle between the normal of the face k and the relative velocity of the air, deg
ϑ	=	parameter of a probability density function
$\boldsymbol{\vartheta}$	=	vector of parameters of a probability density function
χ	=	spherical angle (declination) of the ejection velocity, deg
Ω	=	right ascension of the ascending node, deg
$\boldsymbol{\omega}_e$	=	Earth spin vector, rad/s

Subscripts and superscripts

d	=	drag
e	=	relative to the initial orbital eccentricity
g	=	gravitational
h	=	relative to the initial altitude from the equatorial radius
j, k, m	=	generic indexes
i	=	relative to the initial orbital inclination

*Ph.D. Student, Space Structures and Systems Laboratory, Aerospace and Mechanical Engineering Department, Chemin des Chevreuils 1. Student Member AIAA.

†Professor, Stochastic Modeling Laboratory, Aerospace and Mechanical Engineering Department, Chemin des Chevreuils 1.

‡Professor, Space Structures and Systems Laboratory, Aerospace and Mechanical Engineering Department, Chemin des Chevreuils 1.

l	=	relative to the initial conditions prior to ejection and launcher accuracy
max	=	upper bound
min	=	lower bound
n_j	=	relative to the jth gas species
O	=	oxygen
pert	=	perturbation
p	=	perigee
ref	=	reference condition
T	=	relative to the local atmospheric temperature
X	=	relative to the random variable X
0	=	relative to initial conditions

I. Introduction

THE continuing growth of space debris is a problem of great concern to the astrodynamics community. Most national space agencies and the Inter-Agency Space Debris Coordination Committee now firmly accept a maximum orbital lifetime [1]. Specifically, spacecraft must now be able to deorbit within 25 years from protected regions, namely from low Earth orbits (LEO) and geostationary orbits (GEO). Spacecraft most often exploit chemical propulsion for this purpose, although novel deorbiting strategies, including electrical propulsion [2], solar sails [3], and tethers [4], are currently being investigated as well. In other cases, proving through supporting long-term orbit propagations that the natural orbital decay of the spacecraft requires less time than the prescribed 25-year limit may suffice to satisfy the requirement. In this context, the design and optimization of deorbiting strategies require reliable orbital lifetime estimation.

Lifetime estimation began with the early space age with the method developed by Sterne [5], which was based upon analytic expressions for the rate of change of apogee and perigee. Ladner and Ragsdale [6] improved this method and through recommendations in the choice of the most sensitive parameters, they emphasized the importance of uncertainties. Orbital propagation efficiency was then improved by Chao and Platt [7] thanks to a novel set of simplified averaged equations of classical orbital elements. The adequate treatment of atmospheric density led to renewed interest in lifetime estimation. For instance, Fraysse et al. [8] described good practices for lifetime computation of LEO satellites where drag may be significant and introduced the concept of equivalent solar activity.

However, owing to various experimental and modeling limitations, various parametric uncertainties and modeling errors impede accurate orbital lifetime estimation. For example, Monte Carlo simulations performed in the position paper on space debris mitigation [9] indicated that the orbital lifetime of a spacecraft with an initial $36,000 \times 250$ km orbit can vary between about 8 years (with a relative frequency of 5%) to about 70 years (with a relative frequency also of 5%). Oltrogge and Leveque [10] provide another example of the variability of three different lifetime estimation tools in the analysis of orbital decay of CubeSats. Variations of the order of 50% were observed between predicted and observed lifetime.

Dominant sources of parametric uncertainties and modeling errors in orbital lifetime estimation include uncertainties in atmospheric properties, in the initial state of the satellite, and in physical properties of the satellite. First, although remarkable efforts were performed to gain insight into the nature of the atmosphere [11–13], a complete and thorough understanding of the mechanisms that determine the gas composition, the temperature, and other atmospheric properties has not been achieved yet; even if further detailed models were available, their efficient numerical implementation would be prohibitive. In addition, most atmospheric models available in the literature rely on the correlation of the density with solar and geomagnetic activity indicators, which are subject to uncertainties themselves. Next, uncertainty in the initial state of the satellite may arise either because the mission design status, e.g., some initial orbital parameters, is not known yet or because of experimental limitations, e.g., limitations associated with GPS or two-line elements (TLEs) datasets. Finally, uncertainties in the physical properties of the satellite may concern the drag and reflectivity coefficients, the mass, and the geometry.

Although all these uncertainties exist for every mission, their relative importance is case-dependent.

Although there is a large body of literature concerning lifetime estimation, uncertainty quantification (UQ) of orbital propagation is a more recent research topic. By expressing the analytical solution with a Taylor series expansion and by solving the Fokker–Planck equation, Park and Scheeres [14] were able to propagate Gaussian uncertainty in the initial states of a nonlinear deterministic evolution problem. Nonlinear dynamics propagation resulted in a progressive distortion of the probability distribution of the states, which became non-Gaussian. Further work on the propagation of the uncertainty in the initial states by means of the Fokker–Planck equation was performed by Giza et al. [15], who were also able to efficiently propagate uncertainty by considering a simplified drag model. Analytical propagation of uncertainties in the two-body problem was then achieved by Fujimoto et al. [16]. Concerning uncertainty propagation techniques, Jones et al. introduced the polynomial chaos expansion (PCE) method in astrodynamics [17,18]. Important issues in lifetime estimation are summarized by Saleh et al. [19], whereas Scheeres et al. [20] pointed out the existence of a rigorous and fundamental limit in squeezing the state vector uncertainty. In summary, nonlinear and long-period dynamics propagation [21], as well as severe uncertainty sources, make UQ of orbital lifetime a difficult problem.

We view probabilistic UQ of orbital lifetime estimation as a three-step problem. The first step involves using methods from mathematical statistics in conjunction with mechanical modeling considerations to characterize the uncertainties involved in the orbital lifetime estimation problem as one or more random variables. The second step is to map this probabilistic characterization of inputs through the orbital propagator into a probabilistic characterization of the orbital lifetime; this can be achieved in several ways, which include Monte Carlo simulation [22] and stochastic expansion methods such as those based on polynomial chaos [23,24]. The third step involves using the probabilistic model thus obtained to gain insight into the impact that the input uncertainties have on the orbital lifetime, for example, by carrying out stochastic sensitivity analyses. In this paper, we focus on the first step, i.e., the probabilistic characterization of the dominant sources of uncertainty involved in the lifetime estimation of low-altitude satellites. Uncertainties in the initial state of the satellite and in the atmospheric drag force, as well as uncertainties introduced by modeling limitations associated with atmospheric density models, are considered. The proposed probabilistic characterization facilitates the application of uncertainty propagation and sensitivity analysis methods, which we postpone to a companion paper [25].

To illustrate the proposed methodology, the standard two-unit (2U) CubeSat of the QB50 constellation [26] proposed by the von Karman Institute for Fluid Dynamics in Belgium is considered. This case study is particularly relevant for two reasons. First, the objective of the constellation is to study in situ the spatial and temporal variations in the lower thermosphere. The initial circular orbit will have an altitude of 320 km where atmospheric drag, one of the dominant uncertainty sources in astrodynamics, is significant. Second, it is a real-life mission that should be launched in mid-2015; hence, the results described here can be useful not only to the astrodynamics community, but also to the CubeSat developers. The simulation parameters are summarized in Table 1.

The remainder of this paper is organized as follows. Section II details the modeling assumptions and identifies the dominant sources

Table 1   Nominal parameters for simulations

	Variable	Value
Initial conditions	initial altitude	320 km
	eccentricity	0
	orbital inclination	79 deg
	launch date	April 2015
Spacecraft properties	mass	2 kg
	size	0.2 m × 0.1 m × 0.1 m
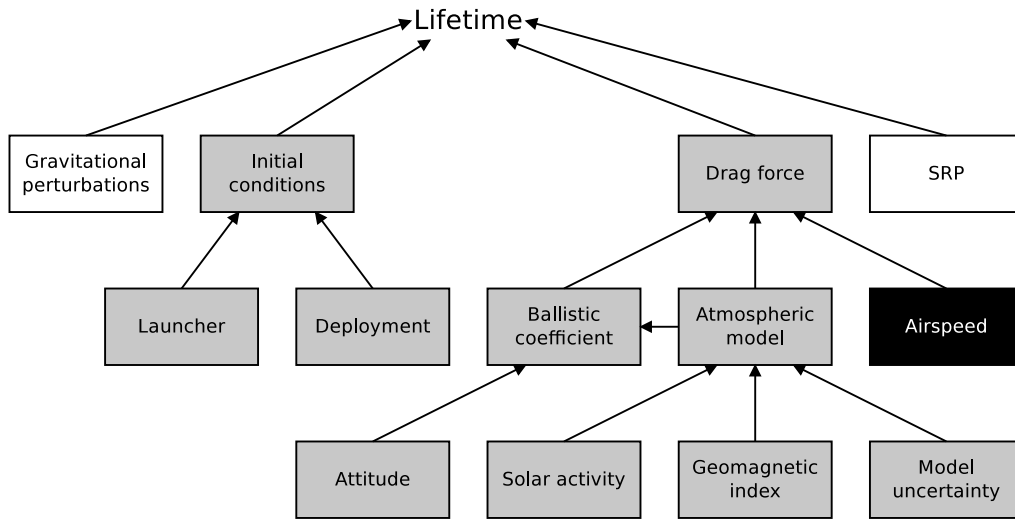
Fig. 1   Schematic representation of UQ of orbital lifetime in LEO. White box: deterministic modeling, gray box: stochastic modeling, black box: unmodeled dynamics.

of uncertainty. Section III summarizes two stochastic methods for uncertainty characterization. Subsequently, the characterization of the uncertainties in the initial conditions and in the drag force is examined in Secs. IV and V, respectively. Finally, Sec. VI briefly discusses the probability density function of the orbital lifetime of a 2U QB50 CubeSat resulting from the propagation of uncertainties carried out in the companion paper.

II.   Modeling Assumptions and Uncertainty Source Identification

The motion of the center of gravity of a nonpropelled Earth orbiting spacecraft is governed by Newton's second law

$$\ddot{r} = -\frac{\nu}{r^3} r + f_{\text{pert}}(r, \dot{r}, t, p, q) \qquad (1)$$

with the following initial conditions

$$r(t_0) = r_0, \quad \dot{r}(t_0) = \dot{r}_0 \qquad (2)$$

here, r is the spacecraft position vector in an Earth centered inertial frame (ECI), $\nu = 3.986 \cdot 10^{14}$ m^{3}s^{-2} is the Earth's gravitational constant, r_0 and $\dot{r}_0$ are the initial position and velocity vectors, respectively, and f_{pert} is the perturbing force per unit mass, which is a function of parameters $p(t)$ and of the spacecraft attitude $q(t)$.

The gravitational constant is known with high accuracy, $\nu = 3.986 \cdot 10^{14}$ m^{3}s$^{-2} \pm 8 \cdot 10^5$ m^{3}s^{-2} [27]; hence, it is supposed to be deterministic in this work. Thus, the uncertainties in the spacecraft dynamics, and, in particular, in the orbital lifetime, originate from the initial conditions and the perturbing forces, as shown in Fig. 1. The main perturbations for a LEO spacecraft are due to the gravity, i.e., nonspherical harmonics of the Earth's gravity field and third-body disturbances of sun and moon f_g to the atmospheric drag f_d and to the solar radiation pressure (SRP) f_{SRP}; hence, $f_{\text{pert}} \simeq f_g + f_d + f_{\text{SRP}}$. Their respective orders of magnitude depend on the considered orbit. Figure 2 illustrates the amplitude of these perturbations for a 2U CubeSat for various LEO altitudes. Minor perturbing forces include radiation pressure of the Earth albedo, which is due to the diffuse reflection of the sunlight, relativistic accelerations, tides, and third-body perturbations of the planets. Nonetheless, they are at least one order of magnitude smaller than SRP, so that their influence can be safely neglected for most applications. Both the Earth's gravitational attraction and third-body perturbations are considered as deterministic quantities in this study because they can be modeled with extremely high accuracy. Concerning the Earth's attraction, Fraysse et al. [8] reported that it is sufficient to include zonal harmonics up to J_4 for lifetime estimation.

Special cases may require a more complete modeling of the perturbing agents. For instance, if sectorial perturbations have very little influence on long-term propagations in LEO, we note that some special orbits could require a more detailed modeling of the gravity field, e.g., it is recommended to include zonal harmonics up to J_{15} for orbits with inclination close to 63.4 deg. Lamy et al. propose a survey of these resonance effects in [28].

Figure 3 provides the numerical evidence that this recommendation is valid for our QB50 case study. Because of the strong nonlinearity of this problem, the convergence of the relative error is not monotonic, especially if zonal-only perturbations are considered. As a result, the relative error tends to stabilize at a value of about 0.1% beyond order 4; this error can be safely neglected with respect to the large uncertainties inherent to orbital lifetime estimation. The modeling of the perturbing force due to SRP is a challenging and demanding task. However, SRP can usually be neglected for low altitudes, as confirmed in Fig. 2, and it is also considered deterministic in this work. We therefore assume in the context of this study that only the perturbations due to atmospheric drag play an important role for UQ of orbital lifetime estimation. Besides the large magnitude of drag perturbations in LEO, this assumption is supported by the fact that drag is uncertain in nature and does not exhibit any relevant compensation throughout one orbit, e.g., it is responsible for a monotonic decrease of the semimajor axis.
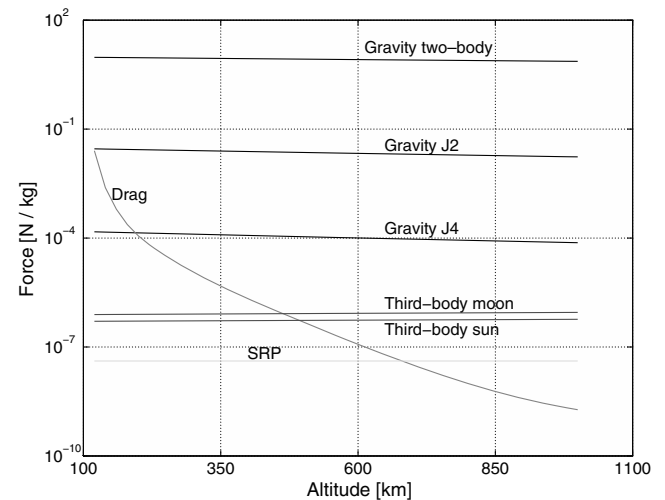
Fig. 2   Order of magnitude of the perturbing forces on a standard QB50 spacecraft.
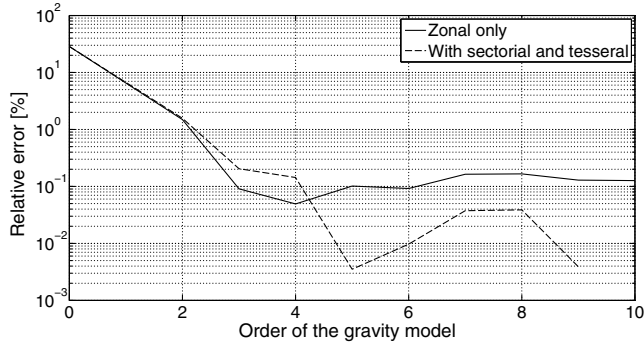
Fig. 3 Error on the orbital lifetime in the nominal case in function of the order of the gravity model.

The popular Runge–Kutta 8(7) [29] is exploited as a numerical integrator for orbital propagation. To reduce the computational burden, we select a relative precision of 10^{-9}, which provides an error of $10^{-2}\%$ with respect to a precision of 10^{-13}.

III. Stochastic Methods for Uncertainty Characterization

Within a probabilistic UQ framework, the objective of characterization is to model the sources of uncertainty involved in the problem under study as one or more random variables X with values in the support I_X. The extension of the methods discussed in this section to the multivariate case is straightforward, but we preferred to illustrate the scalar case to ease the notation. This requires that an adequate probability distribution, or, if X is continuous, its probability density function (PDF) $p_X: I_X \to \mathbb{R}^+$ be assigned to these random variables. The information available for obtaining this distribution typically consists of one or more of the following sources. First, various types of experimental data can be available. Next, there can be mechanical laws that impose constraints on the values that the random variables may take (for example, mechanical laws can require that an uncertain atmospheric density be positive); these constraints act as sources of information because the inferred probability distribution must assign a vanishing probability to those values of the random variables that do not satisfy these constraints. Finally, various other sources can contribute information, for example, in the form of nominal values.

Methods from mathematical statistics are most often used in conjunction with mechanical modeling considerations to infer a characterization of uncertainties from the available information. Providing an exhaustive account of all available methods from mathematical statistics is beyond the scope of this paper; instead, we confine ourselves to a succinct presentation of two fundamental methods.

It is common practice in statistics to use uppercase letters to denote random variables; by contrast, lowercase letters indicate deterministic variables. We use this system of notation in this section, which focuses on the mathematical aspects. However, this rule is not respected elsewhere in the paper, when dealing with physical variables.

A. Maximum Likelihood Estimation

The first method involves selecting an adequate labeled probability distribution, followed by inferring suitable values for its parameters from data, for example, by using the method of maximum likelihood (MLE). By labeled probability distribution we mean Gaussian, uniform, and other probability distributions given in catalogs in the literature. Consider a set of n samples $x_1, \ldots, x_n$ of a random variable X and a PDF $p_X(x; \vartheta_1, \ldots, \vartheta_d)$, where $\vartheta_1, \ldots, \vartheta_d$ are the parameters defining the distribution, e.g., the mean and the standard deviation for the normal distribution. According to the maximum likelihood method, the d parameters of the PDF have to be chosen such that they are consistent, e.g., they have a positive standard deviation, and maximize the likelihood function

$$L(\vartheta_1, \ldots, \vartheta_d) = \prod_{j=1}^{n} p_X(x_j; \vartheta_1, \ldots, \vartheta_d) \quad (3)$$

In practice, the logarithm of the likelihood function is generally considered as the objective function in order to reduce numerical errors due to the product of small numbers.

Care should be taken to select a labeled PDF that is consistent with the physical constraints; for example, the Gaussian probability distribution should not be selected to characterize an uncertain atmospheric density because its support is the whole real line and its selection would thus lead to the assignment of a nonvanishing probability to negative values.

B. Maximum Entropy

If no adequate labeled probability distribution is available, the possibility of constructing a new adequate distribution can be considered, using, for example, the maximum entropy principle [30]. The maximum entropy principle states that the probability distribution with the largest entropy should be selected from among those that are consistent with the available information. The entropy of a continuous random variable X with PDF $p_X(x)$ and support I_X is defined as

$$s_X = -\int_{I_X} p_X(x) \log p_X(x) \, \mathrm{d}x \quad (4)$$

For most of the sources of uncertainty that we characterize using the principle of maximum entropy, the probability distribution is obtained as the one that maximizes entropy

$$\max_{p_X} s_X(p_X) \quad (5)$$

from among those that are consistent with available information of the following form

$$\int_{I_X} p_X(x) \, \mathrm{d}x - 1 = 0, \quad \int_{I_X} x p_X(x) \, \mathrm{d}x - \mu_X = 0,$$
$$\int_{I_X} (x - \mu_X)^2 p_X(x) \, \mathrm{d}x - \sigma_X^2 = 0 \quad (6)$$

here $I_X = [x_{\min}, x_{\max}]$, μ_X and σ_X are a given support, a given mean, and a given standard deviation, respectively. The exact analytical solution to this constrained optimization problem can be obtained using Lagrange multipliers, and it is the truncated Gaussian distribution with support I_X and with second-order statistical descriptors μ_X and σ_X. We stress that these are the second-order descriptors of the actual PDF, i.e., the truncated normal distribution, and not of the associated unbounded normal distribution

$$p_X(x; \tilde{\mu}_X, \tilde{\sigma}_X, x_{\min}, x_{\max}) = \frac{1}{\tilde{\sigma}_X} \frac{p_N\left(\frac{x - \tilde{\mu}_X}{\tilde{\sigma}_X}\right)}{c_N\left(\frac{x_{\max} - \tilde{\mu}_X}{\tilde{\sigma}_X}\right) - c_N\left(\frac{x_{\min} - \tilde{\mu}_X}{\tilde{\sigma}_X}\right)} \quad (7)$$

Here, p_N, c_N, $\tilde{\mu}_X$, and $\tilde{\sigma}_X$ are the PDF and the cumulative distribution function (CDF) of the standard Gaussian distribution and the parameters of the associated unbounded Gaussian distribution, respectively. Here, $\tilde{\mu}_X$ and $\tilde{\sigma}_X$, are obtained by solving

$$\tilde{\mu}_X + [p_X(x_{\min}) - p_X(x_{\max})]\tilde{\sigma}^2 = \mu_X,$$
$$[1 + (x_{\min} - \tilde{\mu}_X)p_X(x_{\min}) - (x_{\max} - \tilde{\mu}_X)p_X(x_{max})$$
$$- (p_X(x_{\min}) - p_X(x_{\max}))^2 \tilde{\sigma}_X^2]\tilde{\sigma}_X^2 = \sigma_X^2 \quad (8)$$

where the dependency of p_X on its parameters are omitted for the sake of conciseness.

For more general applications of the maximum entropy principle, the numerical solution of the problem is an alternative. An interesting
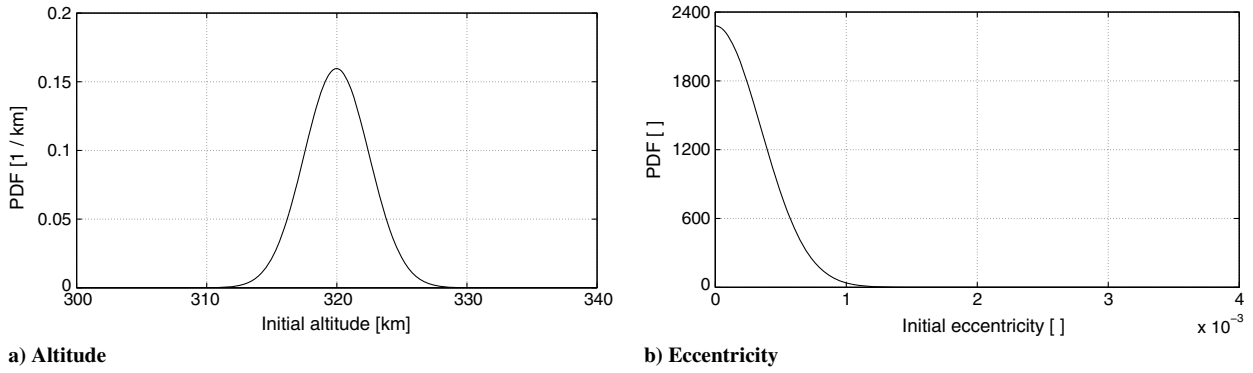
a) Altitude   **b) Eccentricity**

Fig. 4   PDF of the initial altitude and eccentricity prior to deployment (maximum entropy principle).

approach that is particularly suitable for high-dimensional problems was proposed by Soize [31]. A simple numerical implementation is proposed in the Appendix and it is illustrated for the characterization of the initial altitude.

IV. Uncertainty Characterization of Initial Conditions

As discussed in Sec. II, the two main sources of uncertainties considered in the present study are those in the initial states and atmospheric drag. Uncertainty characterization of the initial states is strongly related to the current status of the mission. Two scenarios may occur.

The spacecraft is in orbit. The uncertainty in the initial states depends on measured data, whereas the initial epoch can generally be considered as deterministic. TLEs and GPS are two common measurement techniques. The former is responsible for wider dispersion than the latter, but it is often the only option available for debris and nanosatellites. Relevant work on TLEs uncertainty was performed by Vallado [32] and Flohrer et al. [33]. Kahr et al. [34] estimated the uncertainty in the TLE's positioning of nano and microsatellites by means of GPS data. In the same paper, it is shown that the exploitation of intermittent GPS data, in conjunction with TLEs, can enhance the accuracy of few-day predictions by one order of magnitude.

The mission is still in a design phase, which is the scenario studied in this paper. In this case, uncertainty in the initial states is related to the launch vehicle injection accuracy and to the deployment strategy. The set of nominal initial conditions may also not be fully defined, e.g., the initial right ascension of the ascending node (RAAN) may be unknown.

For the QB50 network, the reference initial conditions prior to the deployment are $h_{0,l}^{ref} = 320$ km, $i_{0,l}^{ref} = 79$ deg, and $e_{0,l}^{ref} = 0$ [26], where $h_{0,l}^{ref}$, $i_{0,l}^{ref}$, and $e_{0,l}^{ref}$ are the initial altitude above the equatorial radius, the orbital inclination, and the eccentricity, respectively. Keplerian elements are used for orbit parametrization because the true anomaly is the only fast variable in this parameter set. Mean elements, instead of osculating elements, are considered to avoid an important sensitivity of the lifetime with respect to the initial anomaly resulting from short-period variations of the semimajor axis. Doing so, we can remove the initial anomaly from the uncertainty sources. Because the reference orbit is circular, the characterization of the initial argument of perigee is not relevant either. As no information is available yet, the initial RAAN is modeled as an aleatory variable with uniform uncertainty between 0 and 360 deg, in accordance with the maximum entropy principle.

The uncertainty in $h_{0,l}$, $i_{0,l}$, and $e_{0,l}$ depends on the accuracy of the launcher. Standard deviations of the Keplerian elements consistent with the performance of current launchers used for LEO are considered, namely, $\sigma_h = 2.5$ km, $\sigma_i = 0.03$ deg, and $\sigma_e = 3.5 \cdot 10^{-4}$. These three variables are supposed to be independent because no information about their correlation is usually provided, and univariate PDFs are constructed in the following.

The initial altitude of the spacecraft is a nonnegative random variable, so that its support is $\mathbb{R}^+$. The mean and standard deviation of the PDF are constrained to be equal to the nominal values $h_{0,l}^{ref}$ and σ_h,

respectively. Thus, according to the maximum entropy principle, $h_{0,l}$ is modeled as a truncated Gaussian distribution with support $\mathbb{R}^+$ and with the imposed second-order descriptors, as shown in Fig. 4a. A similar problem is solved for the initial orbital eccentricity (Fig. 4b) and inclination. For these variables, the support is $[0,1]$ and $\mathbb{R}$, respectively.

The initial date t_0 is the last parameter necessary to fully define the initial state prior to the deployment of the constellation. The launch is foreseen for April 2015 [26]. However, because of the frequent delays in space missions, t_0 is modeled as a uniform random variable between April 1, 2015 and April 1, 2016. A wider launch window is not necessary, because the long-term variations in the atmospheric models are not considered herein.

A second source of uncertainty for the initial conditions is the deployment of the QB50 constellation. Even though the exact strategy for deployment is still unknown, the nanosatellites will be ejected thanks to a spring-loaded pusher plate with an ejection velocity between 1 and 1.5 ms^{-1}. Though negligible with respect to the orbital speed, the ejection velocity may be responsible for uncertainties of the order of launcher accuracy. For example, an ejection velocity in the flight direction leads to an increment of the semimajor axis of 2.6 km, which is larger than σ_h. Therefore, the ejection velocity is modeled as a vector with norm v_{ej} and direction uniformly distributed in $[1.0, 1.5]$ ms^{-1} and in the space, respectively. Parameterizing the direction with azimuth Θ and elevation χ yields

$$p_{\Theta,\chi}(\Theta,\chi) = \frac{1}{360}\frac{\cos \chi}{2} \text{ [deg}^{-2}] \quad (9)$$

Here, Θ and χ are defined in $[0, 360]$ deg and $[-90, 90]$ deg, respectively. This distribution is uniform over the radian sphere and it is obtained by considering that the infinitesimal surface with these parameters is given by $\cos \chi d\Theta d\chi$.

V. Uncertainty Characterization of Atmospheric Drag

The second main source of uncertainty considered in this paper is the atmospheric drag. The drag force per unit of mass is computed using the empirical equation

$$f_d = -\frac{1}{2}C_b \rho v_{TAS} \mathbf{v}_{TAS} \quad (10)$$

where C_b, ρ, v_{TAS}, and $\mathbf{v}_{TAS}$ are the ballistic coefficient, the atmospheric density, the true airspeed (TAS), and its modulus, respectively. According to Vallado and Finkleman [35], all the terms involved in Eq. (10) and the equation itself are affected by uncertainties.

In this paper, the TAS is calculated using the assumption of a corotating atmosphere

$$\mathbf{v}_{TAS} = \dot{\mathbf{r}} - \boldsymbol{\omega}_E \times \mathbf{r} \quad (11)$$

where $\boldsymbol{\omega}_E$ is the Earth's angular velocity. This means that we do not consider the upper-thermosphere winds, which can be of the order of

several hundreds of meters per second [36–38]. However, the basic dynamics of the wind involve a movement from daylight to nighttime, which approximately results in a compensation of their effects throughout one orbit. Relevant work on the determination of these winds from experimental data is performed in [39], and different models are available in the literature [40,41]. The thermospheric cooling trend [42] is also ignored herein.

We stress that the drag force is just one component of the aerodynamic force. Lift and side forces are also considered in our simulations, although their orders of magnitude and influence on lifetime are much smaller.

A. Atmospheric Model

The dominant uncertainty source in the drag estimation is the atmospheric density. One of the most advanced atmospheric models is NRLMSISE-00, which is a global, i.e., from ground to exosphere, empirical model developed by the U.S. Naval Research Laboratory. The model is calibrated by means of mass spectrometer, incoherent scatter, and accelerometer measurements. Two important inputs of the model are the daily and 81-day averaged radio flux indices, $F_{10.7}$ and $\bar{F}_{10.7}$. The 3-hour geomagnetic index a_p is another input of the model, but, for long-period propagations, its daily average A_p can be exploited. The other inputs required by NRLMSISE-00 are the position of the spacecraft and the Julian date (JD), which are computed throughout the numerical integration of the equations of motion. Although they depend on random variables, e.g., $JD(t) = t + t_0$, they are not primary sources of uncertainty. Given these inputs, NRLMSISE-00 is able to estimate the number densities of helium, atomic and molecular oxygen, atomic and molecular nitrogen, argon, and hydrogen, together with the local atmospheric temperature. The total mass density is deduced directly from these outputs.

1. Solar and Geomagnetic Proxies

Correlation between gas density and space weather proxies, e.g., solar radio flux and geomagnetic index, is crucial in the development of an atmospheric model. The sensitivity of the orbital lifetime with respect to these variables is very substantial [43]. This section focuses on the characterization of the solar and geomagnetic random variables. Different approaches were proposed in the literature to address this important problem. Among them, Ashrafi et al. [44] developed a prediction tool based on chaos theory, and proved that it is more suitable than statistical approaches for short-term prediction. Watari [45] and Loskutov et al. [46] introduced methodologies for the identification of periodic and chaotic components and for solar activity forecasting based on singular spectrum analysis. To generate realizations of realistic future solar flux trajectories (geomagnetic activity was not considered), Woodburn and Lynch [47] proposed to superpose to the trend of the trajectory a scalar exponential Gauss–Markov sequence.

The consideration of time-varying series complicates the uncertainty propagation because the problem belongs to the family of stochastic differential equations [48]. As an alternative for use in orbital lifetime estimation, Fraysse et al. introduced the concept of constant equivalent solar activity [8]. The idea is to consider a constant solar flux and geomagnetic index throughout the propagation. If the satellite has a 25-year lifetime for the chosen constant equivalent solar activity, then its lifetime for possible future solar activities will also be 25 years, with a probability of 50%. The equivalent solar flux is a function of the ballistic coefficient C_b and of the altitude of the apogee h_p, whereas the daily geomagnetic index is set to 15. This technique is particularly appropriate for very long propagations in the order of one or several solar cycles.

In this work, we propose another approach to the problem. It is also based upon the idea of using an effective solar activity, but it is more suitable for propagations of the order of a fraction of the solar cycle. Instead of a deterministic effective solar activity, we consider a random effective solar activity. The main underlying assumption is that neglecting variations of the space weather proxies with respect to their averaged value in time, does not yield drastic variations of the
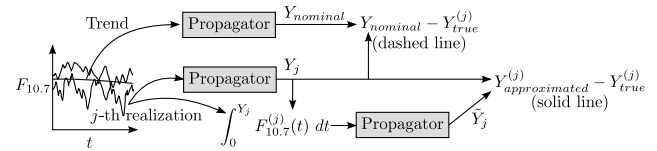
a) Schematic representation of the computation of the error when mean value of each realization is considered
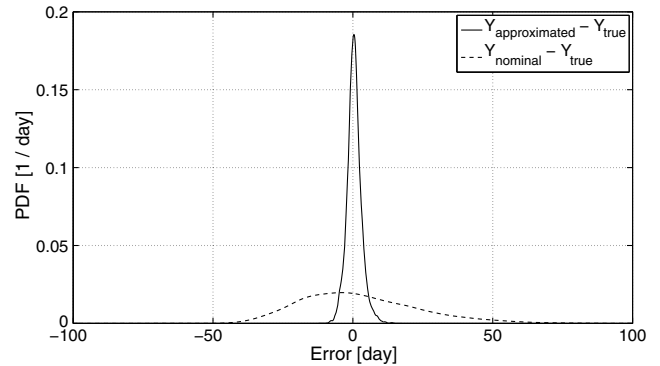
b) Probability distribution of the error

Fig. 5 Comparison between the PDF of the error between true and approximated orbital lifetime (solid curve), and the PDF of the error between true and nominal lifetime (dashed curve).

orbital lifetime. To verify this conjecture, we performed two sets of simulations where the solar activity is modeled by means of 1) time series and 2) its temporal average. Then, we compared the resulting orbital lifetime in the two cases, which, for the sake of clarity, we refer to as true and approximated lifetime, respectively. Specifically, we exploited the stochastic process proposed by Woodburn and Lynch [47] to generate several realizations of the solar activity, and we computed statistics of the difference between the realizations of the true and the approximated lifetime. The schematic representation of this process is illustrated in Fig. 5a. The resulting distribution has a mean value of 0.5 day and a standard deviation of 2.4 days. Finally, we compared this result with the difference between the nominal and the realizations of the true lifetime. The nominal lifetime is computed with the trend of the solar activity according to the long term Schatten's predictions and it is deterministic. This nominal trend is the deterministic component of the time series generated by Woodburn and Lynch [47]. The standard deviation of this difference is one order of magnitude larger than the one of the error between true and approximated lifetime, as illustrated in Fig. 5b. Hence, these results support that $F_{10.7}$, $\bar{F}_{10.7}$, and A_p can be considered in the context of this study as three different random variables that are constant during a single simulation. Their characterization is discussed in the following.

Here, $F_{10.7}$, $\bar{F}_{10.7}$, and A_P are characterized using the data measured over the last 50 years provided by the CelesTrak database [49]. Bearing in mind that QB50 has a lifetime of a few months and that the launch window is [April 2015, April 2016], the portion of the solar cycle between [October 2014, October 2016] is considered to be conservative. Thus, only the data of the previous cycles that correspond to the same portion of the solar cycle are exploited for uncertainty characterization. Because of the important variations in correspondence of the solar maxima and of the variability in the period of the solar activity, the identification of the selected dataset is achieved by identifying the minima of the solar flux curve smoothed by a moving-average filter of 2-year width. These minima are then used to define a dimensionless position between two consecutive minima of the solar cycle. This process is illustrated for the daily solar flux in Fig. 6; a similar process can be carried out for $\bar{F}_{10.7}$ and A_p. The data in the shaded windows are retained for uncertainty characterization of the solar weather proxies.

Figures 7 and 8 illustrate the correlations between the retained datasets of the three proxies and their marginal distributions (histograms in Fig. 8), respectively. The statistical model must be able
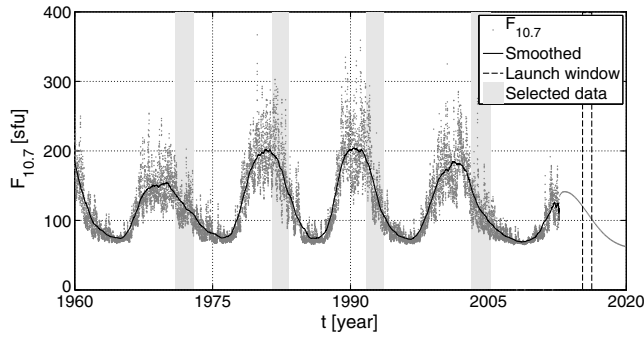
Fig. 6 Observed daily solar activity.

to represent both the marginal distributions of and the correlation between the three variables. For this purpose, $F_{10.7}$, $\bar{F}_{10.7}$, and A_P are modeled by the following Gaussian copula [50]

$$
\left.\begin{array}{c} Z_1 \\ Z_2 \\ Z_3 \end{array}\right\} \xrightarrow{\text{chol}(C)} \left\{\begin{array}{c} \Xi_1 \xrightarrow{c_N(\xi_1)} U_1 \xrightarrow{\mathcal{F}_{F_{10.7}}^{-1}(u_1;\vartheta_{F_{10.7}})} F_{10.7} \\ \Xi_2 \xrightarrow{c_N(\xi_2)} U_2 \xrightarrow{\mathcal{F}_{\bar{F}_{10.7}}^{-1}(u_2;\vartheta_{\bar{F}_{10.7}})} \bar{F}_{10.7} \\ \Xi_3 \xrightarrow{c_N(\xi_3)} U_3 \xrightarrow{\mathcal{F}_{A_p}^{-1}(u_3;\vartheta_{A_p})} A_p \end{array}\right. \quad (12)
$$

Here, Z_1, Z_2, and Z_3 are independent standard Gaussian random variables, Ξ_1, Ξ_2, and Ξ_3 are correlated standard Gaussian random variables, and $\text{chol}(C)$ is the Cholesky decomposition of their correlation matrix. It yields $[\Xi_1, \Xi_2, \Xi_3] = [Z_1, Z_2, Z_3]\text{chol}(C)$, U_1, U_2, and U_3 are correlated uniform random variables with support $[0,1]$, $\mathcal{F}_{(\cdot)}$ is the cumulative distribution function CDF of the marginal distribution that is chosen to fit the model, and $\vartheta_{(\cdot)}$ is the vector of parameters defining the distribution.

The identification of the parameters of the statistical model is achieved by means of the MLE, as described in Sec. III.A. The design variables of the MLE problem are the parameters of the marginal PDFs and the three off-diagonal elements of the correlation matrix

$$
\begin{aligned} & p_{F_{10.7},\bar{F}_{10.7},A_p} \\ & = p_{F_{10.7},\bar{F}_{10.7},A_p}(F_{10.7}, \bar{F}_{10.7}, A_p; \vartheta_{F_{10.7}}, \vartheta_{\bar{F}_{10.7}}, \vartheta_{A_p}, C_{1,2}, C_{2,3}, C_{3,1}) \end{aligned}
$$
$$(13)$$

Physical constraints impose that the chosen distributions of the solar flux indices are defined on $\mathbb{R}^+$, whereas the support of the geomagnetic indicator is $[0,400]$.

Several labeled PDFs and nonparametric histogram distributions were tested to model the marginal PDFs. On the one hand, labeled distributions are interesting because the resulting model can be tuned with a very limited number of parameters. On the other hand, histogram distributions are able to represent, with the highest fidelity, the statistical content of the dataset, but several parameters are necessary to tune the model, i.e., the heights of each bin.
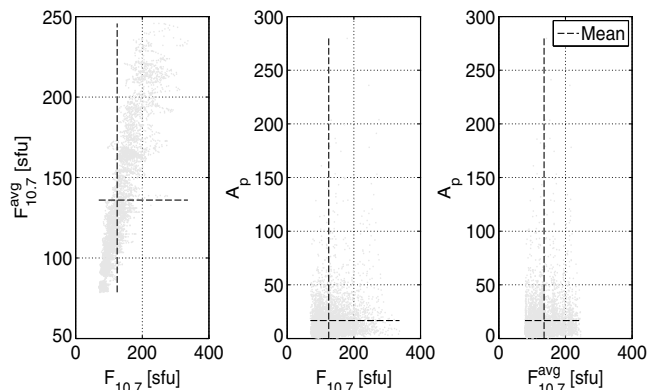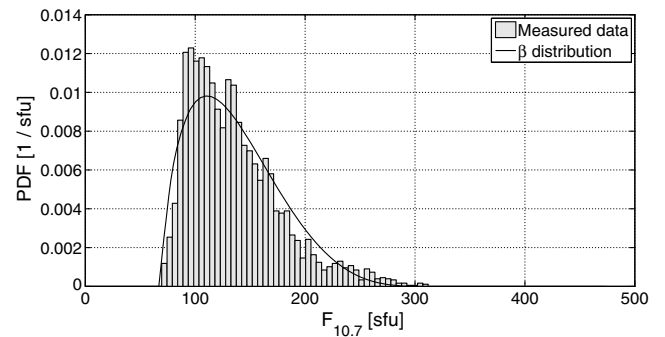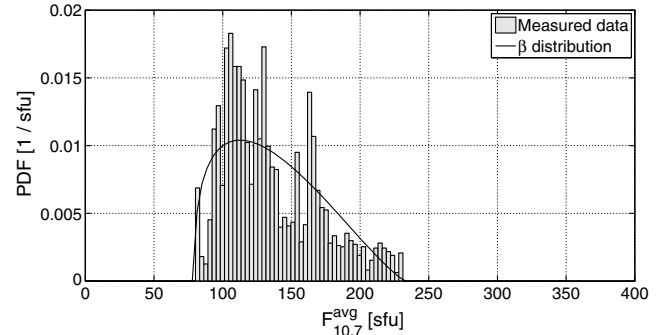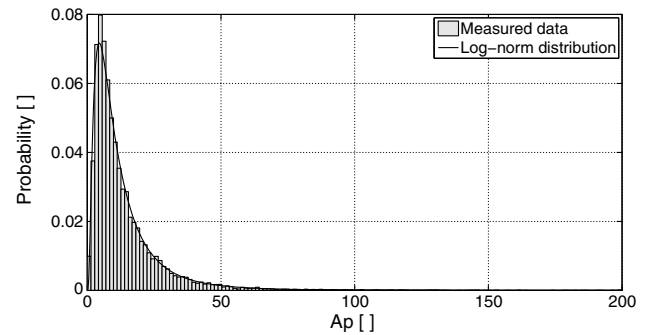

Fig. 7 Correlation between the solar flux and geomagnetic indices.

a) Daily $F_{10.7}$

b) 81-day averaged $F_{10.7}$

c) Geomagnetic activity A_p

Fig. 8 Distributions of the geomagnetic and solar activity proxies (maximum likelihood).

Among the different labeled distributions we tested, beta distributions generated the maximum likelihood. However, the histogram model performed better. This result is illustrated in Fig. 8, which presents the beta and histogram marginal PDFs for the three variables. If the distributions of $F_{10.7}$ and A_p appear to be sufficiently well fitted by the beta distributions, this is not the case for $\bar{F}_{10.7}$, and histogram distributions for the marginal PDFs are retained.

2. Model Uncertainty

Targeting practicality and efficient numerical computation, the most popular atmospheric models exploit a limited number of proxies to take the correlation between density and stochastic processes into account. This is why the uncertainty characterization of the density should also consider the uncertainty related to the discrepancy of the model with respect to reality. For instance, Scholz et al. compared the atmospheric densities given by different models including NRLMSISE-00, DTM-2009, JB-2008, and GITM [51]. They observed deviations in the order of 50% considering the same environmental conditions. In addition to the discrepancies among different models, Pardini et al. [52], Bowman and Moe [53], and Bowman and Hrncir [54] studied the biases of different models by comparing physical and fitted drag coefficients. Overestimation of the density at low altitude was observed for all the models, with peaks of the order of 20%. The oversimplified physical drag modeling

exploited for the tuning of old models and the absence of long-term thermospheric cooling are responsible for this systematic overestimation.

To cope with model uncertainty of NRLMSISE-00, the work of Picone et al. [55] is exploited in this paper. They performed a statistical analysis between the NRLMSISE-00 model and experimental data and tabulated the biases and standard deviations of the gas composition and temperature for different ranges of altitudes, for in situ and ground-based measurements, and for quiet ($A_p \leq 10$), active ($A_p \geq 50$), and all geomagnetic conditions. Biases for number density of gas species n_j and for the temperature T are defined as

$$\beta_{n_j}^{(k)} = \exp\left[\mathrm{E}\left(\log \frac{n_j^{(\mathrm{data},k)}}{n_j^{(\mathrm{model})}} \right) \right] - 1 \qquad (14)$$

$$\beta_T^{(k)} = \mathrm{E}\left(T^{(\mathrm{data},k)} - T^{(\mathrm{model})} \right) \qquad (15)$$

respectively. Superscripts model and data correspond to the outputs of the NRLMSISE-00 model and experimental data, respectively. Here, $\mathrm{E}[\bullet]$ denotes the expectation operator with respect to the different measurements within a single dataset, k. The corresponding standard deviations are

$$\sigma_{n_j}^{(k)} = \sqrt{ \mathrm{E}\left(\log^2 \frac{n_j^{(\mathrm{data},k)}}{n_j^{(\mathrm{model})}} \right) - \log^2(\beta_{n_j}^{(k)} + 1) } \qquad (16)$$

$$\sigma_T^{(k)} = \sqrt{ \mathrm{E}\left(\left(T^{(\mathrm{data},k)} - T^{(\mathrm{model})} \right)^2 \right) - \beta_T^{(k)2} } \qquad (17)$$

In what follows, the measurements for all levels of geomagnetic activity in the altitude range [200, 400] km are considered. This is where most of the lifetime will be spent in our test case. The residual lifetime below 200 km is in the order of one day. To account for this variability, we define random variables, denoted η_{n_j} and η_T, for each of the outputs of NRLMSISE-00 such that the corrected atmospheric properties are given by

$$n_j = n_j^{(\mathrm{model})} \exp(\eta_{n_j}) \qquad (18)$$

$$T = T^{(\mathrm{model})} + \eta_T \qquad (19)$$

These random variables are considered constant throughout a single orbit propagation. They are characterized using the maximum entropy principle in the following. Because the available information is given in terms of the bias and standard deviation and because their support is $\mathbb{R}$, the random variables η_{n_j} are characterized by a normal distribution with second-order descriptors

$$\mu_{n_j} = \mathrm{E}\left(\log\left(1 + \beta_{n_j}^{(k)} \right) \right) \qquad (20)$$

$$\sigma_{n_j} = \sqrt{ \mathrm{E}\left(\sigma_{n_j}^{(k)2} + \mu_{n_j}^{(k)2} \right) - \mu_{n_j}^2 } \qquad (21)$$

here the expectation operator is with respect to the different datasets.

For the random variable η_T, nonnegativity of the temperatures must be enforced, i.e., $I_{\eta_T} = [-T, \infty)$. The resulting distribution depends on the temperature T and no feasible solution exists for $T < -\beta_T$, β_T being the mean value of $\beta_T^{(k)}$ across the different datasets. In practice, however, this temperature range is not physically meaningful; it is never reached using the NRLMSISE-00 model. The resulting distribution is a truncated Gaussian with left bound equal to $-T$ and second-order descriptors β_T and σ_T. We note that the distributions converge to the unbounded normal distribution for $T \gg -\beta_T + 3\sigma_T$, as illustrated in Fig. 9.
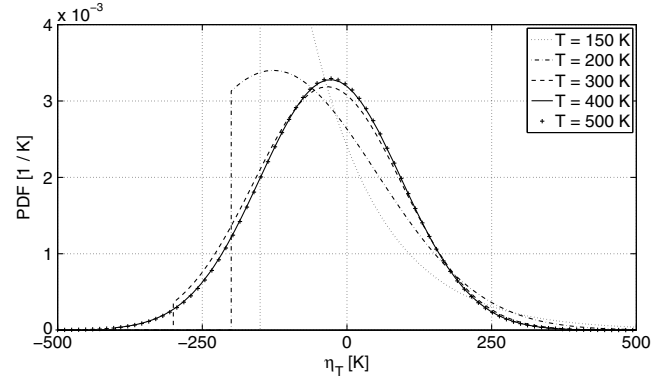
Fig. 9   PDF of the model correction factor of the temperature in function of the external temperature (maximum entropy principle).

The obtained second-order statistical descriptors of η_{n_j} and η_T are listed in Table 2.

B.   Ballistic Coefficient

The computation of the ballistic coefficient

$$C_b = \frac{C_d A_{\mathrm{ref}}}{m} \qquad (22)$$

where C_d, A_{ref}, and m are the dimensionless drag coefficient, the reference surface, and the mass of the spacecraft, respectively, is a very challenging and important problem for LEO propagation. The drag coefficient is itself a function of the atmospheric conditions, i.e., gas composition and external temperature, of the physical properties of the spacecraft, i.e., the mass and geometry, of its attitude, of the wall temperature, and of the gas–surface interaction.

Two complementary approaches exist for the determination of the drag coefficient. The first consists of its computation from observation of the orbital dynamics of the spacecraft, and it is referred to as fitted drag coefficient. This method does not require a physical modeling of the aerodynamic force, but it just assumes an underlying atmospheric model. The result is a coefficient that is consistent with the observed dynamics and that rectifies the bias of the atmospheric model. However, fitted coefficients can be computed only after the launch. The second approach consists of estimating aerodynamic coefficients by means of physical models. This method does not require an atmospheric model and it is appropriate for prelaunch analyses. However, the resulting coefficient can become biased with respect to observations. In this paper, the second approach is considered.

A large body of literature on the determination of physical drag coefficients is available, see [56,57]. For complex satellite geometries, direct simulation Monte Carlo (DSMC), which uses probabilistic Monte Carlo simulations to solve Boltzmann's equation for finite Knudsen number fluid flows, is arguably the only way of computing this coefficient. However, this technique is extremely computationally intensive and does not lend itself to UQ. For simple geometries such as a CubeSat, semi-empirical analytic methods

Table 2   Global biases and standard deviations of the model correction factors of the outputs of NRLMSISE-00 for all levels of geomagnetic activity and an altitude range of [200,400] km

Output	Mean	Std
Temperature, K	−27.9	121.2
Helium, %	8.0	34.7
Total oxygen, %	1.6	25.4
Molecular nitrogen, %	−1.1	35.9
Argon, %	18.6	52.0
Hydrogen, %	4.0	31.4
Atomic nitrogen, %	−15.7	53.0

relying on the decomposition into elementary panels provide an accurate and computationally effective alternative. The semi-analytic method considered in this work is based upon the research of Sentman [58] and Cook [59] and upon the more recent contributions of Moe and Moe [60], Sutton [61], Fuller and Tolson [62], and Pilinski et al. [63]. The method is efficiently summarized in [39].

Consider a one-sided elementary panel, say the kth spacecraft panel, oriented with an angle ψ_k between the bulk velocity of the flow, v, and its normal, and provided with surface A_k. Given the ratio of the bulk velocity to the most probable thermal velocity of the jth gas species

$$W_j = \frac{v}{v_{\mathrm{mp},j}} = v\left(2\frac{BT}{m_j}\right)^{-1/2} \tag{23}$$

where B and m_j are Boltzmann's constant and the molecular mass of the jth species, respectively, the dimensionless drag coefficient is provided by Sentman's formula

$$C_d^{(k,j)} = \left[\frac{P_{k,j}}{\sqrt{\pi}} + \cos\psi_k\left(1 + \frac{1}{2W_j^2}\right)Z_{k,j}\right.$$
$$\left. + \frac{\cos\psi_k}{2}\frac{v_{\mathrm{re}}}{v_{\mathrm{inc}}}\left(\sqrt{\pi}Z_{k,j}\cos\psi_k + P_{k,j}\right)\right]\frac{A_k}{A_{\mathrm{ref}}} \tag{24}$$

with

$$P_{k,j} = \frac{\exp(-W_j^2\cos^2\psi_k)}{S_j}$$

$$Z_{k,j} = 1 + \mathrm{erf}(W_j\cos\psi_k)$$

$$\frac{v_{\mathrm{re}}}{v_{\mathrm{inc}}} = \sqrt{\frac{1}{2}\left(1 + \alpha\left(\frac{4RT_w}{v^2} - 1\right)\right)} \tag{25}$$

where v_{re}, v_{inc}, R, T_w, and α are the velocity of the reemitted particles and of the incoming particles, the specific gas constant, the spacecraft wall temperature, and the energy flux accommodation coefficient, respectively. This latter coefficient is an indicator of the gas–surface interaction. It determines whether the reflected particles retain their mean kinetic energy (for $\alpha = 0$) or they acquire the spacecraft wall temperature T_w (for $\alpha = 1$) [39]. The numerical simulations we carried out pointed out that the term $4RT_wv^{-2}$ is very small with respect to 1. We therefore consider it as deterministic with $T_w = 300$ K. For the energy accomodation coefficient, to our knowledge, data for its stochastic characterization are not available, and we model it as $\alpha = 5.10^{-7}n_OT(1 + 10^{-7}n_OT)^{-1}$, as suggested by Pilinski et al. [64].

Summing up the contributions of the panels with a positive contribution to the drag and of the different gas species, Eq. (22) is recast into

$$C_b = \frac{A_{\mathrm{ref}}}{m}\sum_{k,j}\left(\frac{n_j}{n_{\mathrm{tot}}}C_d^{(k,j)}\right) \tag{26}$$

This equation was used in our orbital propagator to compute the ballistic coefficient at every time step. The main contribution to uncertainty depends on the outputs of the atmospheric model, which were already characterized in the previous section. Another contribution is spacecraft attitude, which determines the angles ψ_k. The requirements for a standard QB50 spacecraft impose that the angle δ between the CubeSat's long axis and the velocity be smaller than 5 deg with $3 - \sigma$ confidence [65]. There is no requirement on the roll angle ϵ. According to the maximum entropy principle, the attitude angles δ and ϵ are modeled as a Gaussian random variable with zero mean and a standard deviation of $5/3$ deg, and a uniform random variable with values in $[0, 360]$ deg, respectively. We emphasize that this analysis does not account for the commissioning, which in the case of QB50 is required to be within the first two

orbiting days. For other spacecraft, commissioning might last several weeks, especially for nanosatellites with limited attitude control. During commissioning, the spacecraft is tumbling and considering this phase would require six degree-of-freedom propagation and the characterization of the initial angular rates, which is beyond the scope of this paper.

We note that the results of the discussed analytic method were compared with full-blown DSMC simulations performed at the von Karman Institute for Fluid Dynamics. Table 3 shows that errors in the order of 1% were achieved, thus validating our approach. Another interesting finding from this table is that the ballistic coefficient is indeed insensitive with respect to wall temperature.

VI. Probability Density Function of Orbital Lifetime

Tables 4 and 5 presents an overview of our characterization of the uncertainty sources affecting the orbital lifetime of the standard QB50 satellite in our study. As already mentioned, we postpone to a

Table 3 Errors between the analytic and DSMC-based numerical predictions for the ballistic coefficient[a]

Altitude, km	Angle of attack, deg	Wall temperature, K	Analytical, C_b [m²/kg]	Relative error, %
120	0.00	273.15	1.21e − 02	0.36
120	0.00	298.15	1.21e − 02	0.38
120	0.00	323.15	1.21e − 02	0.38
120	5.00	273.15	1.34e − 02	1.34
120	5.00	298.15	1.34e − 02	1.33
120	5.00	323.15	1.34e − 02	1.34
120	10.00	273.15	1.51e − 02	0.89
120	10.00	298.15	1.51e − 02	0.86
120	10.00	323.15	1.51e − 02	0.85
120	15.00	273.15	1.69e − 02	1.10
120	15.00	298.15	1.69e − 02	1.08
120	15.00	323.15	1.69e − 02	1.05
200	0.00	273.15	1.33e − 02	−0.03
200	0.00	298.15	1.34e − 02	−0.02
200	0.00	323.15	1.34e − 02	−0.02
200	5.00	273.15	1.46e − 02	3.40
200	5.00	298.15	1.47e − 02	3.39
200	5.00	323.15	1.47e − 02	3.38
200	10.00	273.15	1.59e − 02	0.66
200	10.00	298.15	1.59e − 02	0.66
200	10.00	323.15	1.60e − 02	0.65
200	15.00	273.15	1.76e − 02	0.03
200	15.00	298.15	1.76e − 02	0.04
200	15.00	323.15	1.76e − 02	0.04
280	0.00	273.15	1.38e − 02	0.01
280	0.00	298.15	1.38e − 02	0.01
280	0.00	323.15	1.38e − 02	−0.01
280	5.00	273.15	1.51e − 02	4.11
280	5.00	298.15	1.51e − 02	4.10
280	5.00	323.15	1.52e − 02	4.09
280	10.00	273.15	1.63e − 02	1.22
280	10.00	298.15	1.63e − 02	1.21
280	10.00	323.15	1.63e − 02	1.22
280	15.00	273.15	1.79e − 02	0.16
280	15.00	298.15	1.79e − 02	0.16
280	15.00	323.15	1.79e − 02	0.16
350	0.00	273.15	1.40e − 02	−0.02
350	0.00	298.15	1.40e − 02	−0.01
350	0.00	323.15	1.41e − 02	−0.01
350	5.00	273.15	1.54e − 02	4.43
350	5.00	298.15	1.54e − 02	4.40
350	5.00	323.15	1.54e − 02	4.41
350	10.00	273.15	1.65e − 02	1.50
350	10.00	298.15	1.65e − 02	1.49
350	10.00	323.15	1.65e − 02	1.49
350	15.00	273.15	1.80e − 02	0.20
350	15.00	298.15	1.80e − 02	0.20
350	15.00	323.15	1.81e − 02	0.21

[a]Full accommodation of the energy is considered for both the analytical and the numerical approaches.

Table 4 Summary of uncertainty characterization

| Variable	Symbol	Units	Stochastic modeling
Launch date	t_0	day	uniform in [1/04/2015, 1/04/2016].
Initial altitude (prior to injection)	$h_{0,l}$	km	truncated Gaussian $[0, +\infty)$, 320 km mean, 2.5 km std
Initial inclination (prior to injection)	$i_{0,l}$	deg	normal with 89 deg mean and 0.03 deg std
Initial eccentricity (prior to injection)	$e_{0,l}$	–	truncated Gaussian $[0, +\infty)$, 0 mean, $3.5 \cdot 10^{-4}$ std
Initial RAAN (prior to injection)	$\Omega_{0,l}$	deg	uniform in [0, 360] deg
Ejection velocity (norm)	v_{ej}	m/s	uniform in [1, 1.5] ms^{-1}
Ejection velocity (azimuth)	Θ	deg	uniform in [0, 360] deg
Ejection velocity (elevation)	χ	deg	cosine distribution in $[-90, 90]$ deg
Daily solar activity	$F_{10.7}$	sfu	histogram distribution (Fig. 8a)
81-day averaged solar activity	$\bar{F}_{10.7}$	sfu	histogram distribution (Fig. 8b)
Geomagnetic index	A_P	–	histogram distribution (Fig. 8c)
Model error of the jth number density	η_{n_j}	–	Gaussian with parameters listed in Table 2
Model error of the temperature	η_T	K	truncated Gaussian, temperature dependent (Fig. 9)
Angle of attack	δ	deg	Gaussian with 0 deg mean and 5/3 deg std
Roll angle	ϵ	deg	uniform in [0, 360] deg

Table 5 Summary of uncertainty correlations

Variables	Correlation, %
$F_{10.7}$ and $\bar{F}_{10.7}$	86
$F_{10.7}$ and A_P	14
$\bar{F}_{10.7}$ and A_P	13

companion paper [25] the propagation of these uncertainties to the orbital lifetime. For completeness, Fig. 10 depicts the PDF obtained in [25] using Monte Carlo simulation. We found a random orbital lifetime with a mean value of 84 days and a standard deviation of 38 days, thus reflecting substantial, but expected, uncertainty. In addition, the lifetime can be as short as 14 days and as long as 347 days depending on the sample considered. These results are clearly of great significance both for mission designers and satellite operators.

Because lifetime has a large standard deviation, a well-converged Monte Carlo propagation is expensive. This is why stochastic collocation techniques are also considered in [25] for uncertainty propagation.

VII. Conclusions

The present study performed a probabilistic characterization of the dominant sources of uncertainty involved in the lifetime estimation of
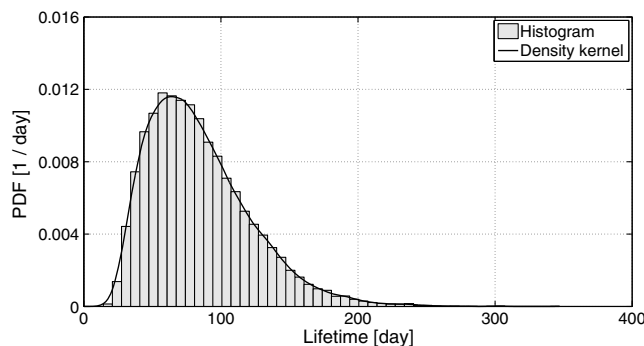
Fig. 10 PDF of the orbital lifetime for a QB50 CubeSat [25].

low-altitude satellites. The developments were illustrated using one CubeSat of the QB50 constellation. Uncertainties in the initial state of the satellite and in the atmospheric drag force, as well as uncertainties that may be introduced by atmospheric density models, were considered. Future improvements of the methodology could consider thermospherical winds, the correlation of the atmospheric temperature with solar activity, and the characterization of the initial states measures through TLEs or GPS data. Provided that sufficient information is available, the methodology could also be extended to other quantities of interest, such as, the SRP. The proposed characterization of the space weather proxies is only appropriate for medium-length propagations, where the mission window can be identified within a fraction of the solar cycle. The extension to very long predictions could be investigated through the use of the equivalent solar activity.

The proposed probabilistic characterization facilitates the application of uncertainty propagation and sensitivity analysis methods to allow insight to be gained into the impact that these uncertainties have on the orbital lifetime, as will be described in a companion paper [25].

Appendix: Numerical Implementation of the Maximum Entropy Principle

In this Appendix, a numerical implementation of the principle based on piecewise linear shape functions is carried out. The support $I_X = [x_{\min}, x_{\max}]$ is divided into M uniform intervals of width $\Delta x = \frac{x_{\max} - x_{\min}}{M}$ with nodes $x_0, x_1, \ldots, x_M$. If either $x_{\min}$ or $x_{\max}$ is unbounded, a finite $x_{\min}$ or $x_{\max}$ should be selected such the PDF value at this modified bound is practically zero.

The generic PDF is constructed using linear shape functions $\varphi_i(x)$

$$p_X(x) = \sum_{j=0}^{M} \varphi_j(x) \vartheta_j \tag{A1}$$

where ϑ_j is nonnegative and represents the evaluation of the PDF at node x_j, whereas φ_j is such that

$$\varphi_0(x) = \begin{cases} \frac{x_1 - x}{\Delta x} & \text{if } x_0 \le x < x_1 \\ 0 & \text{otherwise} \end{cases}$$

$$\varphi_j(x) = \begin{cases} \frac{x - x_{j-1}}{\Delta x} & \text{if } x_{j-1} \le x < x_j \\ \frac{x_{j+1} - x}{\Delta x} & \text{if } x_j \le x < x_{j+1} \quad \text{for } j = 1, \ldots, M-1 \\ 0 & \text{otherwise} \end{cases}$$

$$\varphi_M(x) = \begin{cases} \frac{x - x_{M-1}}{\Delta x} & \text{if } x_{M-1} \le x \le x_M \\ 0 & \text{otherwise} \end{cases} \tag{A2}$$

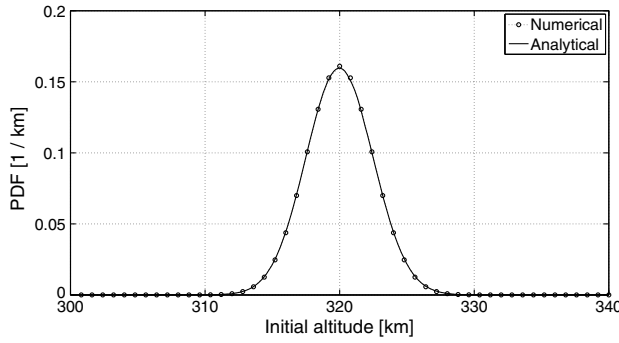According to Eq. (4), the entropy of the synthesized PDF is

$$S_X = -\frac{\Delta x^2}{4} \sum_{j=1}^{M} S_{X,j} \tag{A3}$$

where

$$S_{X,j} = \begin{cases} 0 & \text{if } \vartheta_j = \vartheta_{j-1} = 0 \\ 2\vartheta_j(3 \log(\vartheta_j \Delta x) - 1) & \text{if } \vartheta_j = \vartheta_{j-1} \\ \frac{\vartheta_j^2(2 \log(\vartheta_j \Delta x) - 1) - \vartheta_{j-1}^2(2 \log(\vartheta_{j-1} \Delta x) - 1)}{\vartheta_j - \vartheta_{j-1}} & \text{otherwise} \end{cases} \tag{A4}$$

Equations (5) and (6) are therefore recast into

$$\max_{\vartheta_0, \ldots, \vartheta_M} S_X(\vartheta_0, \ldots, \vartheta_M) \text{ s.t.} \tag{A5}$$

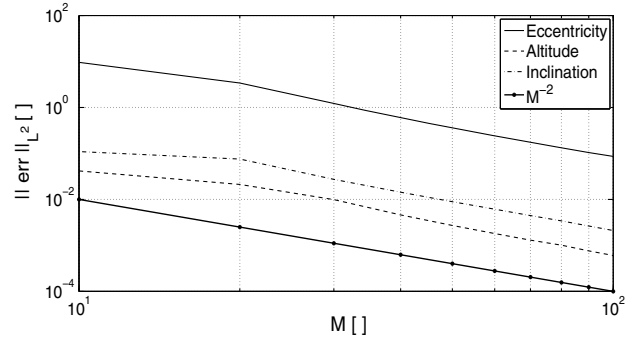**a) Probability distribution for the initial altitude prior to ejection**

b) Convergence of the PDFs identified with the numerical implementation of the maximum entropy method in function of the number of intervals, _M_

Fig. 11 Numerical implementation of the maximum entropy principle.

$$I_X = \int_{I_X} p_X(x; \vartheta_0, \ldots, \vartheta_M)\, dx = \Delta x \left(\frac{\vartheta_0}{2} + \sum_{j=1}^{M-1} \vartheta_j + \frac{\vartheta_M}{2} \right) = 1 \tag{A6}$$

$$\vartheta_j \geq 0 \qquad j = 0, \ldots, M \tag{A7}$$

$$z(\vartheta_0, \ldots, \vartheta_M) \geq \mathbf{0} \tag{A8}$$

$$g(\vartheta_0, \ldots, \vartheta_M) = \mathbf{0} \tag{A9}$$

Equations (A6) and (A7) impose that p_X satisfies the properties of a PDF, whereas the available information related to the specific problem is expressed by Eqs. (A8) and (A9). For instance, the moments of the distribution are often known and can be expressed in terms of the shape functions. For the second-order descriptors, it follows that

$$\mu_X = \frac{1}{\Delta x} \sum_{j=1}^{M} \left[\left(\frac{x_j^3}{6} - \frac{x_j x_{j-1}^2}{2} + \frac{x_{j-1}^3}{3} \right) \vartheta_{j-1} + \left(\frac{x_{j-1}^3}{6} - \frac{x_{j-1} x_j^2}{2} + \frac{x_j^3}{3} \right) \vartheta_j \right] \tag{A10}$$

$$\begin{aligned}
\sigma_X^2 = \frac{1}{\Delta x} \sum_{j=1}^{M} &\left[\left(-\frac{1}{4} x_{j,j-1}^4 + \frac{2\mu_X + x_j}{3} x_{j,j-1}^3 \right.\right. \\
&\left. - \frac{2\mu_X x_j - \mu_X^2}{2} x_{j,j-1}^2 + \mu_X^2 x_j x_{j,j-1}^1 \right) \vartheta_{j-1} \\
&+ \left(\frac{1}{4} x_{j,j-1}^4 - \frac{2\mu_X + x_{j-1}}{3} x_{j,j-1}^3 \right. \\
&\left.\left. + \frac{2\mu_X x_{j-1} - \mu_X^2}{2} x_{j,j-1}^2 - \mu_X^2 x_{j-1} x_{j,j-1}^1 \right) \vartheta_j \right]
\end{aligned} \tag{A11}$$

where $x_{j,m}^k = x_j^k - x_m^k$. All the other constraints of the problem should also be expressed as a function of the design variables $\vartheta_0, \ldots, \vartheta_M$.

This implementation through linear shape functions turned out to be computationally effective in our simulations, as discussed in Secs. IV and V, but it can also be extended to any suitable family of shape functions.

Figure 11 displays the application of the method to the initial altitude prior to ejection and the weighted divergence

$$\sqrt{\int_{\mathcal{R}} (p_{\bar{X}}(\bar{x}) - \tilde{p}_{\bar{X}}(\bar{x}))^2 \tilde{p}_{\bar{X}}(\bar{x})\, d\bar{x}} \quad \text{with } \bar{X} = \frac{X}{\sigma_X} \tag{A12}$$

between the discrete PDFs $p_{\bar{X}}(\bar{x})$ computed using the numerical implementation of the maximum entropy principle and the analytical solution $\tilde{p}_{\bar{X}}(\bar{x})$. We note that this norm attributes high weights to

errors corresponding to high probabilities. The figure shows that the convergence rate is quadratic for the three cases. We note that the solution of the optimization problem showed no sensitivity to the initial guess.

References

[1] "IADC Space Debris Mitigation Guidelines," _40th Session of the Scientific and Technical Subcommittee of the United Nations Committee on Peaceful Uses of Outer Space_, A/AC.105/C.1/L.260, Vienna, Austria, 2003.

[2] Ryden, K., Fearn, D., and Crowther, R., "Electric Propulsion: A Solution to End-of Disposal of Satellites?" _Proceedings of the 2nd European Conference on Space Debris_, ESA, ESOC, Darmstadt, Germany, 1997, pp. 709–712.

[3] Johnson, L., Whorton, M., Heaton, A., Pinson, R., Laue, G., and Adams, C., "NanoSail-D: A Solar Sail Demonstration Mission," _Acta Astronautica_, Vol. 68, No. 5–6, 2011, pp. 571–575.
doi:10.1016/j.actaastro.2010.02.008

[4] Bombardelli, C., Zanutto, D., and Lorenzini, E., "Deorbiting Performance of Bare Electrodynamic Tethers in Inclined Orbits," _Journal of Guidance, Control, and Dynamics_, Vol. 36, No. 5, 2013, pp. 1550–1556.

[5] Sterne, T. E., "An Atmospheric Model and Some Remarks on the Inference of Density from the Orbit of a Close Earth Satellite," _American Astronomical Society_, Vol. 63, 1958, pp. 81–87.
doi:10.1086/107696

[6] Ladner, J. E., and Ragsdale, G. C., "Earth Orbital Satellite Lifetime," NASA TN-D-1995, 1964.

[7] Chao, C. C., and Platt, M. H., "An Accurate and Efficient Tool for Orbit Lifetime Predictions," _Proceedings of the 1st AAS/AIAA Annual Spaceflight Mechanics Meeting_, AAS, Houston, 1991, pp. 11–24.

[8] Fraysse, H., Morand, V., Le Fevre, C., Deleflie, F., Wailliez, S., Lamy, A., Martin, T., and Perot, E., "Long Term Orbit Propagation Techniques Developed in the Frame of the French Space Act," _Proceedings of the 22nd International Symposium on Space Flight Dynamics_, ESA, San Jose dos Campos, Brazil, 2011, pp. 89–105.

[9] "Position Paper on Space Debris Mitigation," International Academy of Astronautics ESA-SP-1301, 2006.

[10] Oltrogge, D., and Leveque, K., "An Evaluation of CubeSat Orbital Decay," _Proceedings of the 25th Annual AIAA/USU Conference on Small Satellites_, AIAA Paper SSC11-VII-2, Logan, 2011.

[11] Jacchia, L. G., "Static Diffusion Models of the Upper Atmosphere with Empirical Temperature Profiles," _Smithsonian Contributions to_

Astrophysics, Vol. 8, No. 9, 1965, pp. 213–257.
10.5479/si.00810231.8-9.213

[12] Jacchia, L. G., "Revised Static Models of the Thermosphere and Exosphere with Empirical Temperature Profiles," Smithsonian Astrophyical Observatory Special Rept. 332, 1971.

[13] Hedin, A. E., "Extension of the MSIS Thermosphere Model into the Middle and Lower Atmosphere," *Journal of Geophysical Research: Space Physics*, Vol. 96, A2, 1991, pp. 1159–1172.
doi: 10.1029/90JA02125

[14] Park, R. S., and Scheeres, D. J., "Nonlinear Mapping of Gaussian State Uncertainties: Theory and Applications to Spacecraft Trajectory Design," *Journal of Guidance, Control and Dynamics*, Vol. 29, No. 6, 2006, pp. 1367–1375.
doi:10.2514/1.20177

[15] Giza, D., Singla, P., and Jah, M., "An Approach for Nonlinear Uncertainty Propagation: Application to Orbital Mechanics," *Proceedings of the AIAA Guidance, Navigation, and Control Conference*, AIAA Paper 2009-6082, Chicago, 2009.

[16] Fujimoto, K., Scheeres, D. J., and Alfriend, K. T., "Analytical Nonlinear Propagation of Uncertainty in the Two-Body Problem," *Journal of Guidance, Control, and Dynamics*, Vol. 35, No. 2, 2012, pp. 497–509.
doi:10.2514/1.54385

[17] Jones, B. A., Doostan, A., and Born, G. H., "Nonlinear Propagation of Orbit Uncertainty Using Non-Intrusive Polynomial Chaos," *Journal of Guidance, Control, and Dynamics*, Vol. 36, No. 2, 2013, pp. 430–444.
doi:10.2514/1.57599

[18] Jones, B. A., Doostan, A., and Born, G. H., "Conjunction Assessment Using Polynomial Chaos Expansions," *Proceedings of the 23rd International Symposium and Space Flight Dynamics*, Jet Propulsion Laboratory, Pasadena, 2012.

[19] Saleh, J. H., Hastings, D. E., and Newman, D. J., "Spacecraft Design Lifetime," *Journal of Spacecraft and Rockets*, Vol. 39, No. 2, 2002, pp. 244–257.
doi:10.2514/2.3806

[20] Scheeres, D. J., Hsiao, F. Y., Park, R. S., Villac, B. F., and Maruskin, J. M., "Fundamental Limits on Spacecraft Orbit Uncertainty and Distribution Propagation," *Journal of the Astronautical Sciences*, Vol. 54, Nos. 3–4, 2006, pp. 505–523.
doi:10.1007/BF03256503

[21] Junkins, J. L., Akella, M. R., and Alfriend, K. T., "Non-Gaussian Error Propagation in Orbital Mechanics," *Journal of the Astronautical Sciences*, Vol. 44, No. 4, 1996, pp. 541–563.

[22] Robert, C. P., and Casella, G., *Monte Carlo Statistical Methods*, 2nd ed., Springer–Verlag, Berlin, 2004, pp. 79–122.

[23] Ghanem, R., and Spanos, P., *Stochastic Finite Elements: a Spectral Approach*, Dover, New York, 2003, pp. 79–122.

[24] Le Maitre, O., and Knio, O., *Spectral Methods for Uncertainty Quantification: With Applications to Computational Fluid Dynamics*, Springer–Verlag, Berlin, 2010, pp. 28–38.

[25] Dell'Elce, L., and Kerschen, G., "Probabilistic Assessment of the Lifetime of Low-Earth-Orbit Spacecraft: Uncertainty Propagation and Sensitivity Analysis," *Journal of Guidance, Control, and Dynamics*, 2013, (submitted for publication).

[26] Muylaert, J., Reinhard, R., and Asma, C., "QB50: An International Network of 50 Cubesats for Multi-Point, In-Situ Measurements in the Lower Thermosphere, and for Re-Entry Research," *Proceedings of the ESA Atmospheric Science Conference*, ESA, Barcelona, Spain, 2009.

[27] Ries, J. C., Eanes, R. J., Shum, C. K., and Watkins, M. M., "Progress in the Determination of the Gravitational Coefficient of the Earth," *Geophysical Research Letters*, Vol. 19, No. 6, 1992, pp. 529–531.
doi:10.1029/92GL00259

[28] Lamy, A., Morand, V., Le Fèvre, C., and Fraysse, H., "Resonance Effects on Lifetime of Low Earth Orbit Satellites," *Proceedings of the 23rd International Symposium on Space Flight Dynamics*, Jet Propulsion Laboratory, Pasadena, 2012.

[29] Montenbruck, O., and Gill, E., *Satellite Orbits. Models, Methods, Applications*, Springer–Verlag, Berlin, 2005, pp. 118–131.

[30] Shannon, C., "A Mathematical Theory of Communication," *Bell System Technical Journal*, Vol. 27, No. 3, 1948, pp. 379–423.
doi:10.1002/bltj.1948.27.issue-4

[31] Soize, C., "Construction of Probability Distributions in High Dimension Using the Maximum Entropy Principle: Applications to Stochastic Processes, Random Fields and Random Matrices," *International Journal for Numerical Methods in Engineering*, Vol. 76, No. 10, 2008, pp. 1583–1611.
doi:10.1002/nme.v76:10

[32] Vallado, D. A., "Verifying Observational Data for Real-World Space Situational Awareness," *Proceedings of the AAS/AIAA Astrodynamics Specialist Conference*, AAS Paper 2011-439, Girdwood, 2011.

[33] Flohrer, T., Krag, H., and Klinkrad, H., "Assessment and Categorization of TLE Orbit Errors for the US SSN Catalogue," *Proceedings of the Advanced Maui Optical and Space Surveillance Technologies Conference*, Maui Economic Development Board, Inc., Maui, 2008.

[34] Kahr, E., Montenbruck, O., and O'Keefe, K., "Estimation and Analysis of Two-Line Elements for Small Satellites," *Journal of Spacecraft and Rockets*, Vol. 50, No. 2, 2013, pp. 433–439.
doi:10.2514/1.A32352

[35] Vallado, D. A., and Finkleman, D., "A Critical Assessment of Satellite Drag and Atmospheric Density Modeling," *Proceedings of the AIAA/ AAS Astrodynamics Specialist Conference*, AIAA Paper 2008-6442, Honolulu, 2008.

[36] Hausler, K., Luhr, H., Rentz, S., and Kohler, W., "A Statistical Analysis of Longitudinal Dependences of Upper Thermospheric Zonal Winds at Dip Equator Latitudes Derived from CHAMP," *Journal of Atmospheric and Solar-Terrestrial Physics*, Vol. 69, No. 12, 2007, pp. 1419–1430.
doi:10.1016/j.jastp.2007.04.004

[37] Wu, Q., Killeen, T. L., and Spencer, N. W., "Dynamics Explorer 2 Observations of Equatorial Thermospheric Winds and Temperatures: Local Time and longitudinal Dependencies," *Journal of Geophysical research*, Vol. 99, No. 5, 1994, pp. 6277–6288.
doi:10.1029/93JA02521

[38] Liu, H., Luhr, H., Watanabe, S., Kohler, W., Henize, V., and Visser, P., "Zonal Winds in the Equatorial Upper Thermosphere: Decomposing the Solar Flux, Geomagnetic Activity, and Seasonal Dependencies," *Journal of Geophysical Research: Space Physics*, Vol. 111, No. A7, 2006.

[39] Doornbos, E., *Thermospheric Density and Wind Determination from Satellite Dynamics*, Springer–Verlag, Dordrecht, 2012, pp. 71–87, 91–121.

[40] Hedin, A. E., Spencer, N. W., and Killeen, T. L., "Empirical Global Model of Upper Thermosphere Winds Based on Atmosphere and Dynamics Explorer Satellite Data," *Journal of Geophysical Research: Space Physics*, Vol. 93, No. A9, 1988, pp. 9959–9978.
doi:10.1029/JA093iA09p09959

[41] Killeen, T. L., Roble, R. G., and Spencer, N. W., "A Computer Model of Global Thermospheric Winds and Temperatures," *Advances in Space Research*, Vol. 7, No. 10, 1987, pp. 207–215.
doi:10.1016/0273-1177(87)90094-9

[42] Emmert, J. T., Picone, J. M., and Meier, R. R., "Thermospheric Global Average Density Trends, 1967–2007, Derived from Orbits of 5000 Near-Earth Objects," *Geophysical Research Letters*, Vol. 35, No. 5, 2008.
doi:10.1029/2007GL032809

[43] Naasz, B. J., Berry, K., and Schatten, K., "Orbit Decay Prediction Sensitivity to Solar Flux Variations," *Proceedings of the AAS/AIAA Space Flight Mechanics Conference*, AAS Paper 2007-264, Mackinac, 2007.

[44] Ashrafi, S., Roszman, L., and Cooley, J., "Nonlinear Techniques for Forecasting Solar Activity Directly From Its Time Series," *Proceeding of the Flight Mechanics/Estimation Theory Symposium*, NASA, 1993, pp. 319–335.

[45] Watari, S., "Separation of Periodic, Chaotic, and Random Components in Solar Activity," *Journal of Solar Physics*, Vol. 168, No. 2, 1996, pp. 413–422.
doi:10.1007/BF00148065

[46] Loskutov, A., Istomin, I. A., Kuzanyan, K. M., and Kotlyarov, O. L., "Testing and Forecasting the Time Series of the Solar Activity by Singular Spectrum Analysis," *Nonlinear Phenomena in Complex Systems*, Vol. 4, No. 1, 2001, pp. 47–57.

[47] Woodburn, J., and Lynch, S., "A Numerical Study of Orbit Lifetime," *Proceedings of the AAS/AIAA Astrodynamics Specialists Conference*, AAS Paper 2005-297, Lake Tahoe, 2005.

[48] Øksendal, B., *Stochastic Differential Equations: An Introduction with Applications*, 5th ed., Springer–Verlag, Heidelberg, New York, 2003, pp. 1–6.

[49] CelesTrak Database, Data available online at http://www.celestrak.com/ SpaceData/sw19571001.txt [retrieved 1 April 2013].

[50] Härdle, W., and Simar, L., *Applied Multivariate Statistical Analysis*, 2nd ed., Springer–Verlag, Berlin, 2007, pp. 119–141.

[51] Scholz, T., Asma, C. O., and Aruliah, A., "Recommended Set of Models and Input Parameters for the Simulations of Orbital Dynamics of the QB50 CubeSats," *Proceedings of the 5th International Conference on Astrodynamics Tools and Techniques*, ESA, Noordwijk, The Netherlands, 2012.

[52] Pardini, C., Moe, K., and Anselmo, L., "Thermospheric Density Model Biases at the 23rd Sunspot Maximum," *Planetary and Space Science*, Vol. 67, No. 1, 2012, pp. 130–146.
doi:10.1016/j.pss.2012.03.004

[53] Bowman, B. R., and Moe, K., "Drag Coefficient Variability at 175–500 km from the Orbit Decay Analyses of Spheres," *Proceedings of the AIAA/AAS Astrodynamics Specialist Conference*, AAS Paper 2005-257, San Diego, 2005.

[54] Bowman, B. R., and Hrncir, S., "Drag Coefficient Variability at 100–300 km from the Orbit Decay Analyses of Rocket Bodies," *Proceedings of the AIAA/AAS Astrodynamics Specialist Conference*, AAS Paper 2007-262, Mackinac, 2007.

[55] Picone, J. M., Hedin, A. E., Drob, D. P., and Aikin, A. C., "NRLMSISE-00 Empirical Model of the Atmosphere: Statistical Comparisons and Scientific Issues," *Journal of Geophysical Research: Space Physics*, Vol. 107, No. A12, 2002, pp. SIA 15-1–SIA 15-16.
doi:10.1029/2002JA009430

[56] Storz, M. F., Bowman, B. R., Branson, J. I., Casali, S. J., and Tobiska, W. K., "High Accuracy Satellite Drag Model (HASDM)," *Advances in Space Research*, Vol. 36, No. 12, 2005, pp. 2497–2505.
doi:10.1016/j.asr.2004.02.020

[57] Marcos, F. A., "New Satellite Drag Modeling Capabilities," *Proceedings of the 44th AIAA Aerospace Sciences Meeting and Exhibit*, AIAA Paper 2006-470, Reno, 2006.

[58] Sentman, L. H., "Free Molecule Flow Theory and its Application to the Determination of Aerodynamic Forces," Lockheed Missiles and Space Company TR-LMSC-448514, 1961.

[59] Cook, G. E., "Satellite Drag Coefficients," *Planetary and Space Science*, Vol. 13, No. 10, 1965, pp. 929–946.
doi:10.1016/0032-0633(65)90150-9

[60] Moe, K., and Moe, M. M., "Gas–Surface Interactions and Satellite Drag Coefficients," *Planetary and Space Science*, Vol. 53, No. 8, 2005, pp. 793–801.
doi:10.1016/j.pss.2005.03.005

[61] Sutton, E. K., "Normalized Force Coefficients for Satellites with Elongated Shapes," *Journal of Spacecraft and Rockets*, Vol. 46, No. 1, 2009, pp. 112–116.
doi:10.2514/1.40940

[62] Fuller, J. D., and Tolson, R. H., "Improved Method for Estimation of Spacecraft Free-Molecular Aerodynamic Properties," *Journal of Spacecraft and Rockets*, Vol. 46, No. 5, 2009, pp. 938–948.
doi:10.2514/1.43205

[63] Pilinski, M. D., Argrow, B. M., and Palo, S. E., "Drag Coefficients of Satellites with Concave Geometries: Comparing Models and Observations," *Journal of Spacecraft and Rockets*, Vol. 48, No. 2, 2011, pp. 312–325.
doi:10.2514/1.50915

[64] Pilinski, M. D., Argrow, B. M., and Palo, S. E., "Semiempirical Model for Satellite Energy-Accommodation Coefficients," *Journal of Spacecraft and Rockets*, Vol. 47, No. 6, 2010, pp. 951–956.
doi:10.2514/1.49330

[65] "Call for CubeSat Proposals for QB50," Von Karman Institute for Fluid Dynamics, 2012.